VARIFORC processing examples

Magnetofossil-rich sediments

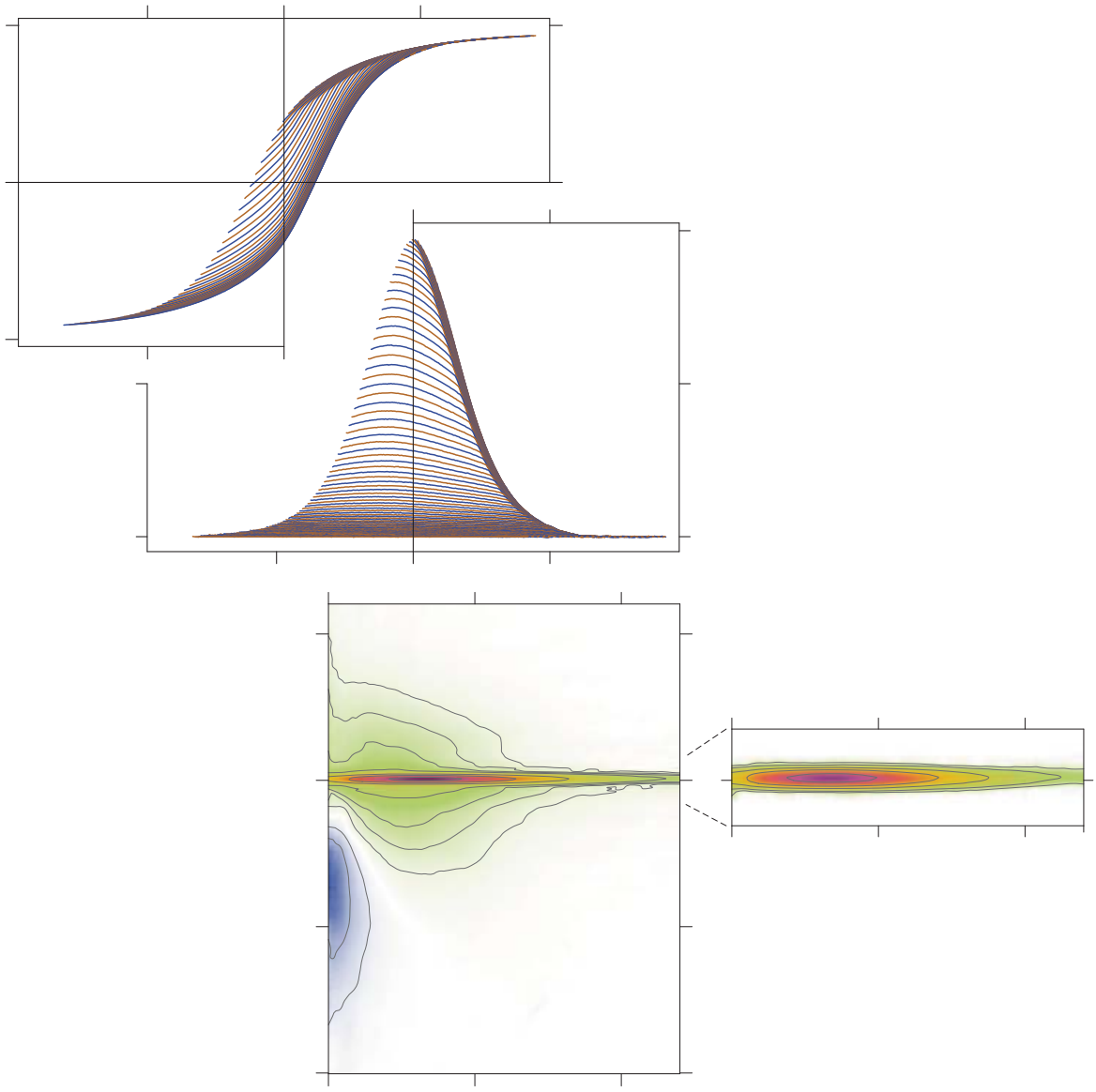

About this example

The measured material is a magnetofossil-bearing pelagic carbonate from the Eastern Equatorial Pacific (2°59.6' S, 110°29'W, 3.87 km water depth) sampled from ODP core 848, Leg 138. High-resolution measurements shown here are part of a study aimed at quantifying secondary magnetite and its intrinsic magnetic signature. Selective chemical dissolution of ultrafine magnetite has been used for this purpose. For further details about this sample, see *Ludwig et al.* [2013]. VARIFORC processing steps are presented in the same sequence as they are usually performed (i.e. import/correct FORC measurements with **`ImportFORC`**, calculate the FORC diagram with **`CalculateFORC`**, isolate the central ridge with **`IsolateCR`**, and combine FORC measurements of different samples with **`LinearCombineFORC`**).

FORC measurements

- Measuring instrument: PMC MicroMag 2900 AGM.
- Specimen mass: 27.2 mg.
- Preparation: Sediment powder fixed with cyanoacrylate glue.
- FORC measurement protocol:

```
Hc1 = 0      , Hc2 = 0.12 T
Hb1 = -0.04 T, Hb2 = +0.06 T
Hsat = 0.3 T
Averaging time       = 0.1 s
Pause at calibration = 0.5 s
Pause at reversals   = 0.5 s
Pause at saturation  = 0.2 s
Smoothing = 5 (adds a 5-point margin to the measured range)
```

- Derived measurement parameters:

```
Number of curves: 450
Calibration measurements at 0.186 T
Mean size of field steps = 0.5 mT (maximum resolution of the FORC diagram)
```

- **Notes on measurements.** AGM measurements tend to be affected by irregular drift. Therefore, it is essential to minimize the total measurement time by choosing a short averaging time (in this example: 0.1 s). Increased measurement noise associated with short averaging times is compensated by repeated measurements (e.g. 2 sets of FORC measurements at 0.1 s averaging time instead of one set at 0.2 s averaging time). Multiple FORC measurements are automatically averaged during VARIFORC processing. In this example, the same specimen has been measured 4 times using the same FORC protocol.

About VARIFORC processing options used in this example

VARIFORC modules are controlled by processing options stored in so-called parameter files. Parameter files used to process FORC data related to this example can be find in the folder containing this document. These are:

1. Import and correct FORC measurements (`ImportFORC` module):

- `S0_VARIFORC_ImportFORC_parameters.txt`: used with data from the untreated material. A first-point correction is applied.
- `S1_VARIFORC_ImportFORC_parameters.txt`: used with data from the CBD-treated material. A first-point correction is applied.

2. Calculate the FORC diagram (`CalculateFORC` module):

- `S0-SF4_VARIFORC_CalculateFORC_parameters.txt`: used with data from the untreated material. A constant smoothing factor (SF = 4) is applied. For demonstration purposes only.
- `S0-SF4-L08_VARIFORC_CalculateFORC_parameters.txt`: used with data from the untreated material. Variable smoothing is applied without taking the central ridge into consideration. For demonstration purposes only.
- `S0-opt_VARIFORC_CalculateFORC_parameters.txt`: used with data from the untreated material, and for the difference between untreated material and CBD-residue. Processing is based on optimized variable smoothing.
- `S1-opt_VARIFORC_CalculateFORC_parameters.txt`: used with data from the CBD-treated material. Processing is based on optimized variable smoothing.

3. Isolate the central ridge (`IsolateCR` module):

- `S0_VARIFORC_IsolateCR_parameters.txt`: used with data from the untreated material, and for the difference between untreated material and CBD-residue.
- `S1_VARIFORC_IsolateCR_parameters.txt`: used with data from the CBD-treated material. `INPUT 01` and `INPUT 02` automatic options for the central ridge range selections have been replaced by manually optimized choices.

Choosing the best FORC measurement range

FORC measurements are time-consuming, so that the measurement protocol range (i.e. `Hc2`, `Hb1`, `Hb2`) must be chosen carefully in order to cover essential features of the FORC diagram without unnecessary measurements over the saturation range of hysteresis. Criteria for the correct choice of measurement parameters are discussed in *Egli et al.* [2010]. The parameters chosen for this example are suitable for a wide range of sediments containing mixtures of magnetofossils and detrital/aeolian inputs (see *Roberts et al.* [2012] for an overview).

VARIFORC can use the whole measurement range to calculate FORC diagrams, instead of the classical rectangular area spanned by the measurement protocol parameters (i.e., H_c comprised between `Hc1` and `Hc2` and H_b comprised between `Hb1` and `Hb2`), so that unnecessary measurements over $H_b < 0$ can be eliminated (Plate 1). In this example, complete coverage of significant FORC diagram features with classical processing would require `Hb1` = −0.22 T instead of −0.13 T, almost doubling the total measurement time. Measurements in this example cover a large range than required by the FORC properties, which were not exactly known at the time the measurements were planned.

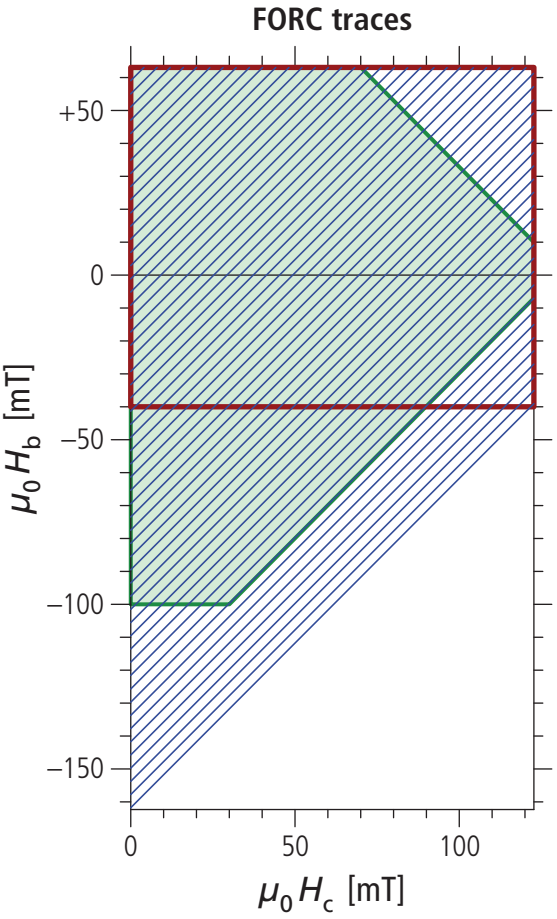

Plate 1. Measurement and output ranges in FORC coordinates. Traces of measured curves are shown as blue diagonal lines (every 8th for clarity). The red rectangle represents the FORC range set by the measurement protocol through `Hc1`, `Hc2`, and `Hb1`, `Hb2`. These parameters are entered with the magnetometer's control software. The red rectangle is also the output range of the FORC diagram obtained with conventional processing software. The VARIFORC output range, on the other hand, can be chosen to include all measurements. The region containing significant FORC contributions is highlighted in green.

FORC measurements

Four sets of identical measurements have been imported and averaged in a single **ImportFORC** run (see parameter file `S0_VARIFORC_ImportFORC_parameters.txt`). This example shows proper unit handling, which was essential for obtaining an estimate of the mass concentration of secondary magnetite. Measurement units, as reported in the measurement file header, were Tesla for the magnetic field and Am^2 for the magnetic moment. The magnetic moment was converted into the SI unit of mass magnetization (mAm^2/kg, see `INPUT 17` of the parameter file), upon normalizing measured magnetic moments by specimen mass (27.2 mg, see `INPUT 16` of the parameter file). The four sets of measurements have been corrected individually for drift and outliers, and subsequently averaged, whereby each set was weighted according to the estimated level of measurement noise, so that worse sets count less than better ones. This procedure minimizes measurement error contributions to the average. In this example, weights of 2.4, 1.4, 0.1, and 0.14, respectively, reflect the heterogeneous quality of the four datasets.

A paramagnetic correction has been applied using the approach-to-saturation method [*Fabian*, 2006] over $|H| \geq 0.13$ T, where hysteresis becomes almost completely closed (see `INPUT 18` of the parameter file). Because this sample contains single-domain particles, the correction uncertainty has been reduced by constraining the approach-to-saturation exponent to its theoretical value of 2 (see `INPUT 20` of the parameter file). Paramagnetic corrections do not affect FORC processing, and are performed only for better representation of ferrimagnetic contributions to the measured curves.

A correction has been applied to the first and last measurement point of each curve (see `INPUT 08` and `INPUT 09` of the parameter file), as the measured magnetization was adversely affected by changes of the field sweep rate occurring at these points. This is a common problem of FORC measurements (see the VARIFORC example on "first point correction"), which is solved by replacing the affected measurements with values extrapolated from adjacent points. Extrapolation is very reliable in case of high-resolution measurements.

Hysteresis parameters (M_{rs}/M_s = 0.42 and H_{cr}/H_c = 1.49) are close to the theoretical values expected for randomly oriented Stoner-Wohlfarth particles, although nominally contained in the so-called pseudo-single-domain range of the Day diagram (Plate 2), where they conform a general trend observed on magnetofossil-bearing sediments. Univocal interpretation of this trend is not possible, as it could be caused by admixtures of one or more of the following: (1) magnetostatic interactions, (2) superparamagnetism, (3) binary mixtures of single-domain and pseudo-single domain/multidomain crystals.

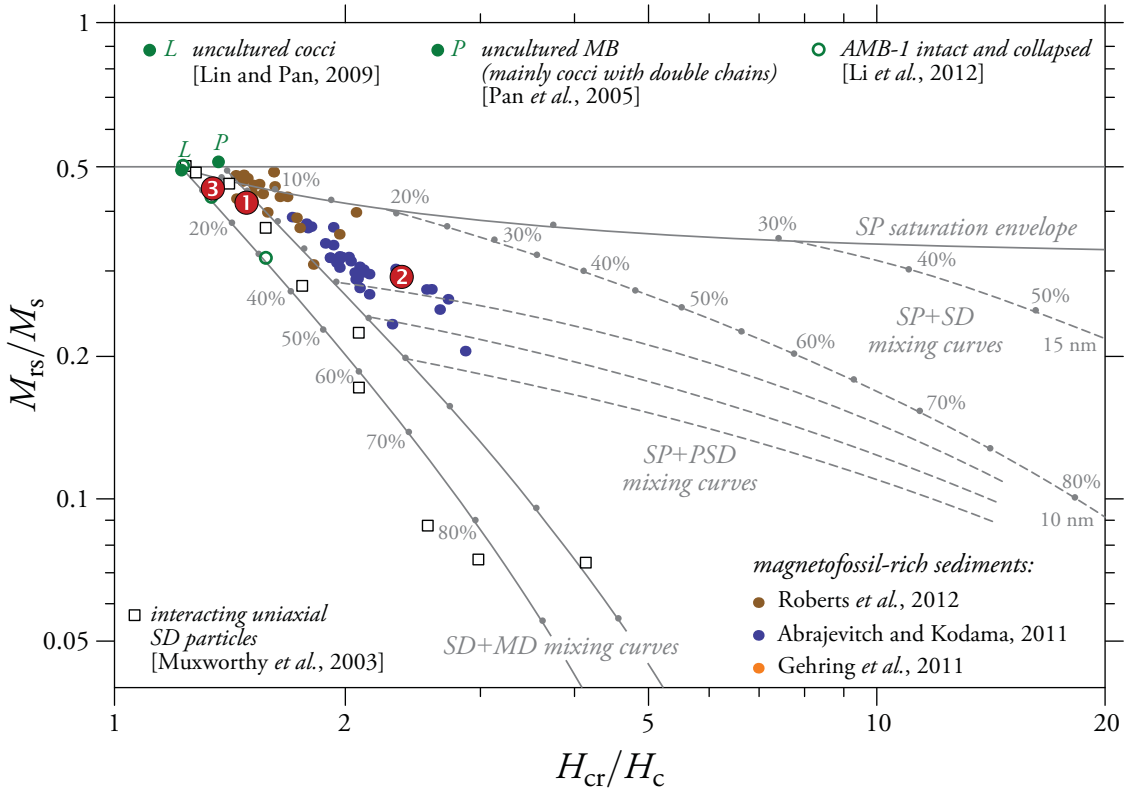

Plate 2. Hysteresis properties in the Day diagram. Day diagram after *Dunlop* [2002] showing the hysteresis properties of magnetofossil-bearing sediments and magnetotactic bacteria samples (dots). Calculated mixing trends are shown in gray. The pelagic carbonate of this example is marked with ❶, the corresponding residue after selective chemical extraction with ❷, and the properties of the extracted particles resulting from the difference between bulk and residue with ❸. The three points define a mixing trend between intact magnetosome chains (green point labeled as *L*) and an unknown end-member nominally equivalent to a mixture of superparamagnetic (SP) and pseudo-single-domain particles (PSD). Magnetofossil-rich sediments (dots) follow the same trend.

FORC measurements plotted by **ImportFORC** reveal additional details about the dominant single-domain nature of this sample (Plate 3). All curves beginning at reversal fields $H_r < 0$ contain a sharp slope discontinuity in proximity of $H = -H_r$ (white line in Plate 3b). This discontinuity creates a sharp horizontal ridge, called the *central ridge*, in the corresponding FORC diagram [*Egli et al.*, 2010]. The central ridge is a characteristic FORC signature of non-interacting single-domain particles [*Newell*, 2005]. Slope discontinuities in the measured curves are captured only with high-resolution FORC measurements at < 1 mT field steps (0.5 mT in this example). The central ridge's sharpness is a key feature enabling accurate quantitative analyses of single-domain magnetic contributions [*Egli et al.*, 2010].

Sediments are often characterized by additional FORC features requiring high-resolution measurements, as for instance zero-coercivity and magnetic viscosity signatures (see the corresponding VARIFORC examples). In general, inspection of measurement plots generated by **ImportFORC** is useful for (1) checking if the chosen measurement range was adequate, (2) identify special features that require careful processing, and (3) obtain additional information about the sample's magnetic properties.

Often, and unlike this example, hysteresis loops of natural samples are almost completely closed, so that measurements are compressed inside the small area between the upper and lower hysteresis branches, where no details can be recognized. Multidomain hysteresis is a paradigm example [*Pike et al.*, 2001]. Especially in these cases, FORC measurements are best represented as differences obtained by subtracting the lower branch of the reconstructed hysteresis loop. The benefit of this representation is also evident in this example (Plate 3c). Measurement differences are part of the default **ImportFORC** output, and, besides offering a better way to inspect results, there are cases where they should be used as source data for the calculation of FORC diagram instead of the original measurements (see example on zero-coercivity contributions).

The envelope of all measurement difference curves coincides with the even component of the hysteresis loop, i.e. the difference between upper and lower branches [*Fabian and Dobeneck*, 1997]. Slope discontinuities caused by the central ridge, as well as other fine details, become particularly evident in plots like Plate 3c.

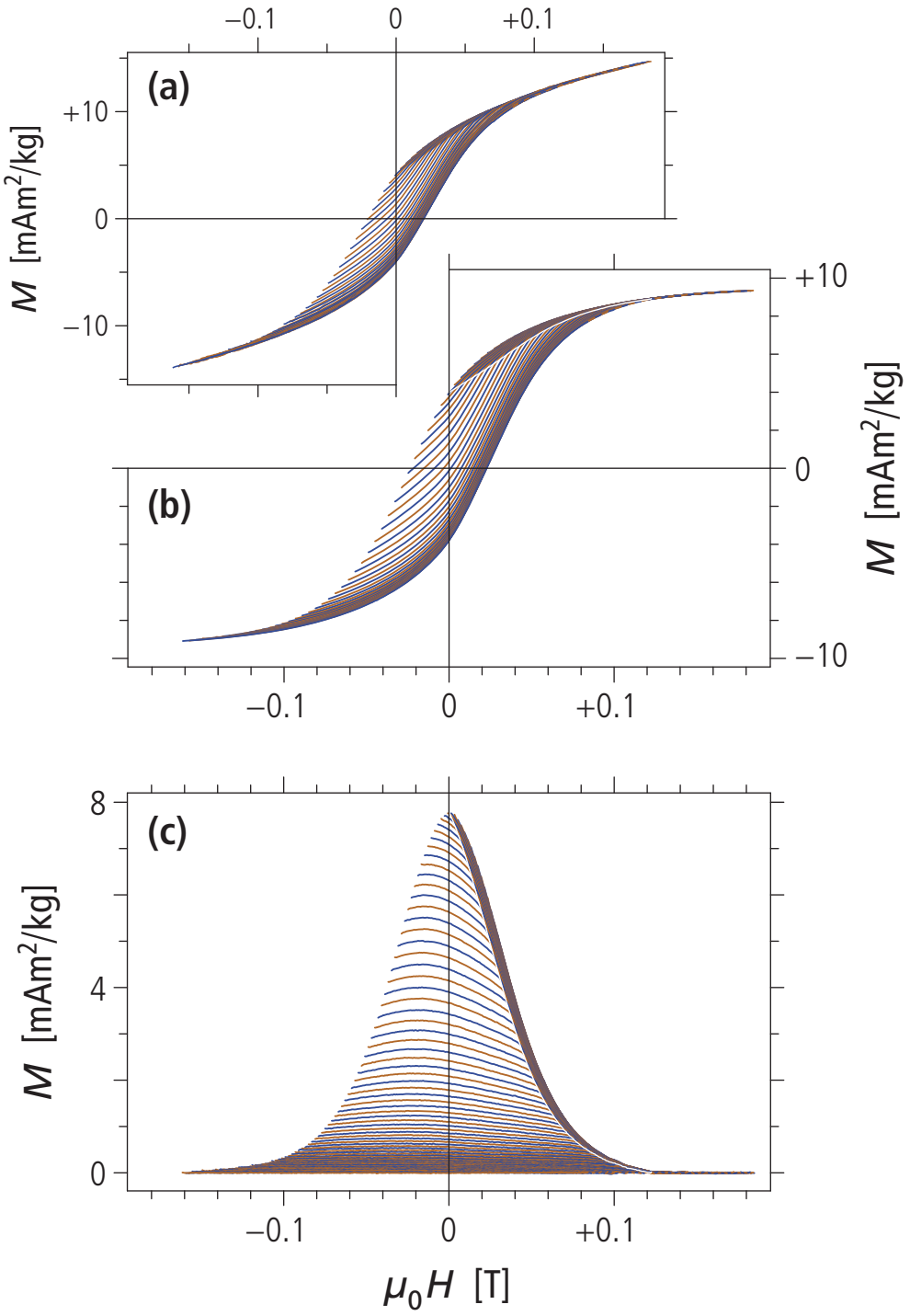

Plate 3. Averaged FORC measurements. Plots were generated by **ImportFORC** with minor editing. **(a)** Weighted average of the four measurement sets after drift and outlier correction. Every 8th curve (see INPUT 14 of the parameter file) is shown for clarity. **(b)** Same as (a), after paramagnetic correction with an approach-to-saturation model based on measurements at field amplitudes ≥0.13 T. The ideal central ridge locus, corresponding to $H = -H_r$, is highlighted by a white line. Sharp slope discontinuities of the measured curves occur just above this line. **(c)** Same as (b), after subtraction of the lower hysteresis branch reconstructed from the FORC measurements (see INPUT 21 of the parameter file). Every 4th curve is shown for clarity. The ideal central ridge locus is highlighted by a white line.

Optimized FORC diagram calculation

FORC diagram calculations for magnetically weak samples, such as the sediment in this example, are best performed with a variable smoothing procedure [*Egli*, 2013], which balances the opposed needs for high resolution and measurement noise suppression over the whole FORC space. The **CalculateFORC** parameter file `S0-opt_VARIFORC_CalculateFORC_parameters.txt` can be used to process high-resolution FORC measurements of most sediments [e.g., *Abrajevitch and Kodama*, 2011; *Roberts et al.*, 2012; *Yamazaki et al.*, 2013; *Chang et al.*, 2014], sedimentary rocks [e.g., *Abrajevitch et al.*, 2011], and soils [*Geiss et al.*, 2008], when focusing on ferrimagnetic contributions. Particular cases requiring a modification of the parameters used here are discussed with specific examples (e.g. "zero-coercivity contributions").

Plate 4 illustrates how best variable smoothing parameters are found in three simple steps. If no previous knowledge about the FORC diagram to be calculated is available (e.g. from similar samples), the first step is based on conventional processing with constant smoothing (Plate 4a-b). In this case, a fixed smoothing factor (e.g. SF = 4, see `INPUT 10-11` in the parameter file `S0-SF4_VARIFORC_CalculateFORC_parameters.txt`) is applied over the whole diagram. High-resolution measurements (i.e., $\delta H \leq 1$ mT) processed with SF ≤ 5 reveal high-amplitude low-dimensional signatures – such as the central ridge of non-interacting single-domain particles or the vertical ridge caused by magnetic viscosity – which require special consideration at later processing steps. On the other hand, low-amplitude regular parts of the FORC diagram are often masked by measurement noise, even when their contribution to the saturation remanence is dominant. This problem is overcome by using smoothing factors that increase when moving away from $H_c = 0$ and $H_b = 0$, starting with a minimum smoothing factor, e.g. SF = 9, which provides the desired measurement noise suppression over the central region of the FORC diagram (Plate 4c-d, see `INPUT 10-11` in the parameter file `S0-SF4-L08_VARIFORC_CalculateFORC_parameters.txt`). Resolution over low-dimensional features, such as the central ridge, is obviously lost at this point, and needs to be recovered by imposing appropriate vertical or horizontal limitations of the smoothing factor. In this example, vertical resolution along the central ridge has been improved by limiting the vertical smoothing factor near $H_b = 0$, in this case to SF = 4 (Plate 4e-f, see `INPUT 13` in the parameter file `S0-opt_VARIFORC_Calculate FORC_parameters.txt`).

As seen later in this example, central ridges found in magnetofossil-bearing sediments are characterized by a small intrinsic vertical width and are shifted upwards with respect to $H_b = 0$. Because these properties are common to all ridges analyzed so far, they can be taken into consideration in order to limit the vertical smoothing factor over an exactly matched region (see `INPUT 13` in the parameter file `S0-opt_VARIFORC_ CalculateFORC_parameters.txt`). The central ridge position and width can be exactly determined with **IsolateCR**.

Details about how to choose smoothing parameters and limit them over specific regions of the FORC diagram are given in the VARIFORC User Manual. In general, a single set of parameters, such as `S0-SF4_VARIFORC_CalculateFORC_parameters.txt` can be used to process whole groups of samples with similar properties, provided that they have been measured with – at least nearly – the same resolution.

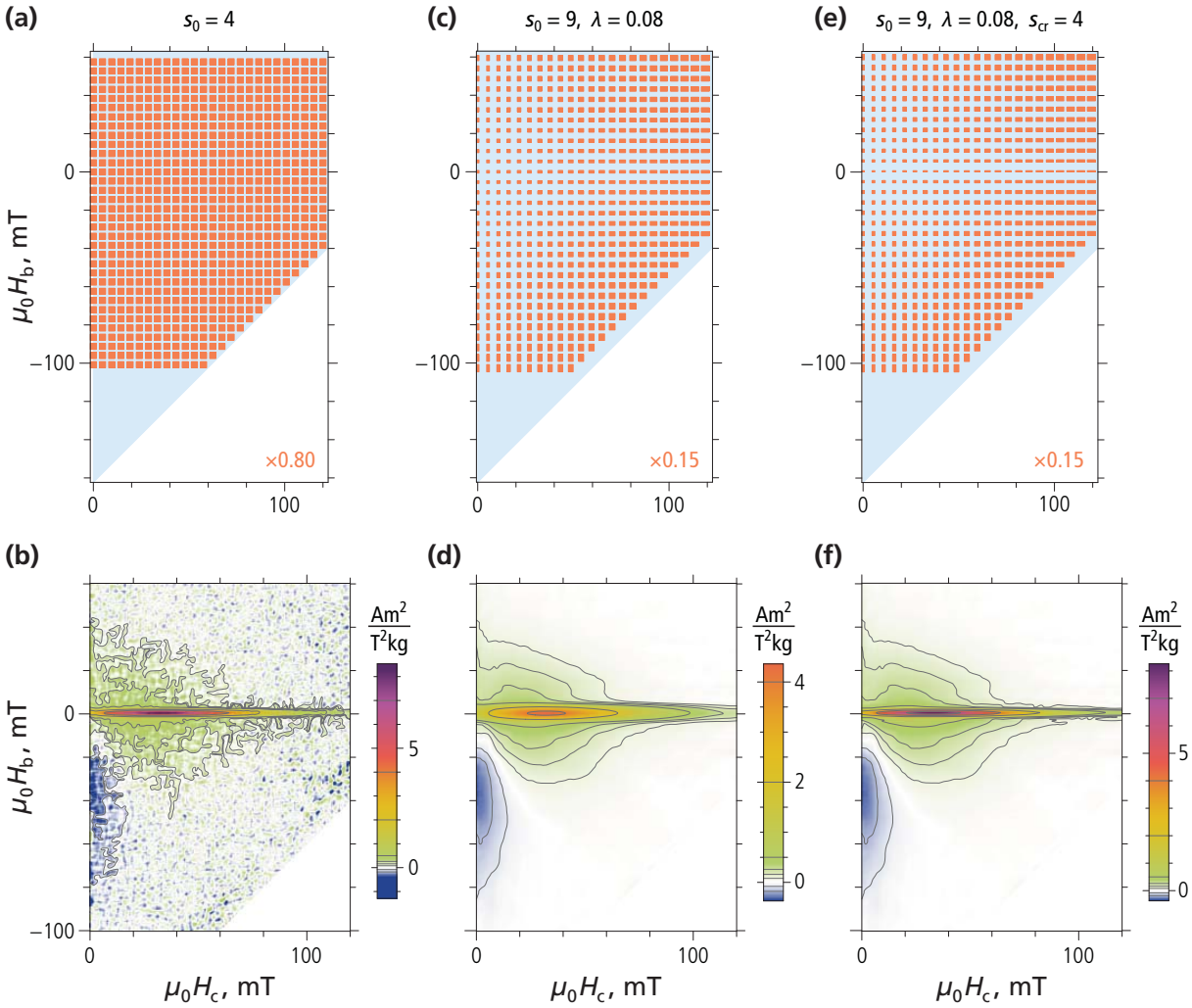

Plate 4. Smoothing parameter optimization with `CalculateFORC`. The top graphics row shows rectangular selections (orange, not to scale) of measurement points (shaded blue area) used for polynomial regression. The size of these rectangular selection is controlled by a horizontal (s_c) and a vertical (s_b) smoothing factor. The bottom graphics row shows the resulting FORC diagrams (contour lines have been added with **`Plot FORC`**). The same color scale has been used for all diagrams. **(a-b)** Conventional processing with a constant smoothing factor SF = 4 (i.e., $s_c = s_b = 0$). The central ridge along $H_b \approx 0$ is correctly resolved, while remaining contributions are dominated by measurement noise, even if contributing to ~44% of the total saturation remanence. **(c-d)** The size of regression rectangles increases proportionally to the distance from the FORC diagram axes, starting from $s_c = 9$ at $H_c = 0$ and $s_b = 9$ at $H_b = 0$. In this example, the increase rates of s_c and s_b are given by $0.08/\delta H$, where $\delta H \approx 0.5$ mT is the field step of measurements. Accordingly, the smoothing factors increase by ~16 over 100 mT. Measurement noise is now adequately suppressed over the whole FORC space at cost of a vertical resolution loss over the central ridge, due to the minimum smoothing factor $s_b = 9$. **(e-f)** Vertical resolution over the central ridge is gained by limiting the vertical smoothing factor along $H_b \approx 0$ to $s_b = 4$. These processing parameters merge the advantages of (b) (i.e., resolution) and (c) (i.e., measurement noise suppression). The relative contribution of the central ridge to the total magnetization associated with the FORC diagram is exactly the same in (d) and (f), despite evident amplitude differences.

Central ridge analysis

The central ridge is a quasi-one dimensional feature of the FORC diagram whose characteristics depend, at least in part, on FORC processing parameters. For example, the ridge amplitude in Plate 4 depends on the vertical smoothing factor used near $H_b = 0$. Because of this dependence on processing parameters, quantitative analysis of FORC diagrams containing a central ridge is possible only through a proper procedure for isolating the ridge and converting it into a regular function, i.e. the central ridge coercivity distribution f_{cr} [*Egli et al.*, 2010; *Egli*, 2013]. This operation is performed with the **IsolateCR** module of VARIFORC, as illustrated in Plate 5 (see also Chapter 6 of the VARIFORC user manual).

The first step of the **IsolateCR** analysis consists in calculating a mean vertical profile across the central ridge (Plate 5b), using data from a selected area of the FORC diagram containing part of the ridge where FORC amplitudes are maximal, as well as its immediate surroundings (Plate 5a). If FORC measurements have been performed with high resolution (i.e., field steps ≤ 1 mT), and the central ridge is a dominant feature, as in this example, this operation can be fully automatized (see `INPUT 01` and `INPUT 02` in the parameter file `S0_VARIFORC_IsolateCR_parameters.txt`). The average profile is then fitted with appropriate model functions for the central ridge (green curve in Plate 5b) and the remaining FORC contributions (gray curve in Plate 5b), providing the initial parameters for performing the same operation for each vertical profile in the FORC diagram. Once all profiles have been modeled, the contribution of the central ridge to each profile can be isolated, obtaining a FORC diagram of the central ridge (Plate 5c). The integral of this function over H_b yields the central ridge coercivity distribution $f_{cr}(H_c)$, which, unlike the central ridge itself, does not depend on processing parameters used to calculate the FORC diagram (Plate 5d).

Real central ridges in FORC diagrams of magnetofossil-bearing sediments are slightly shifted on the vertical direction, with mean position given by $\mu_0 H_b \approx +0.4$ mT (Plate 5e). Also, their vertical width is slightly larger than the width expected from smoothing an infinitely sharp ridge (Plate 5f). Using $\sigma_{CR}^2 = \sigma_i^2 + \sigma_{SF}^2$ for the vertical central ridge standard deviation σ_{CR} resulting from the combination of an intrinsic contribution σ_i and the contribution σ_{SF} introduced by smoothing, we obtain $\sigma_i \approx 0.5$ mT. Upwards shift and intrinsic width can be explained by thermal activation effects [*Egli*, 2006].

The outcomes of central ridge analysis with **IsolateCR** are useful not only for evaluating various types of magnetic contributions in the FORC diagram (see next section), but also for setting optimized processing parameters to be used with **CalculateFORC**, as far as limitations of the vertical smoothing factor over the central ridge are concerned. These limitations apply over a range of H_b-values that is determined by the mean vertical position and intrinsic width of the ridge. In this example, a mean vertical position of +0.4 mT and an intrinsic width of 0.5 mT have been used to calculate the FORC diagram (see `INPUT 13` in the parameter file `S0-opt_VARIFORC_CalculateFORC_parameters.txt`), according to Plate 5e,f. These parameters, expressed in the proper field unit chosen for FORC processing, can be used for any kind of magnetofossil-bearing sediments. In case of unknown central ridge properties, preliminary processing can be used to find optimal parameters.

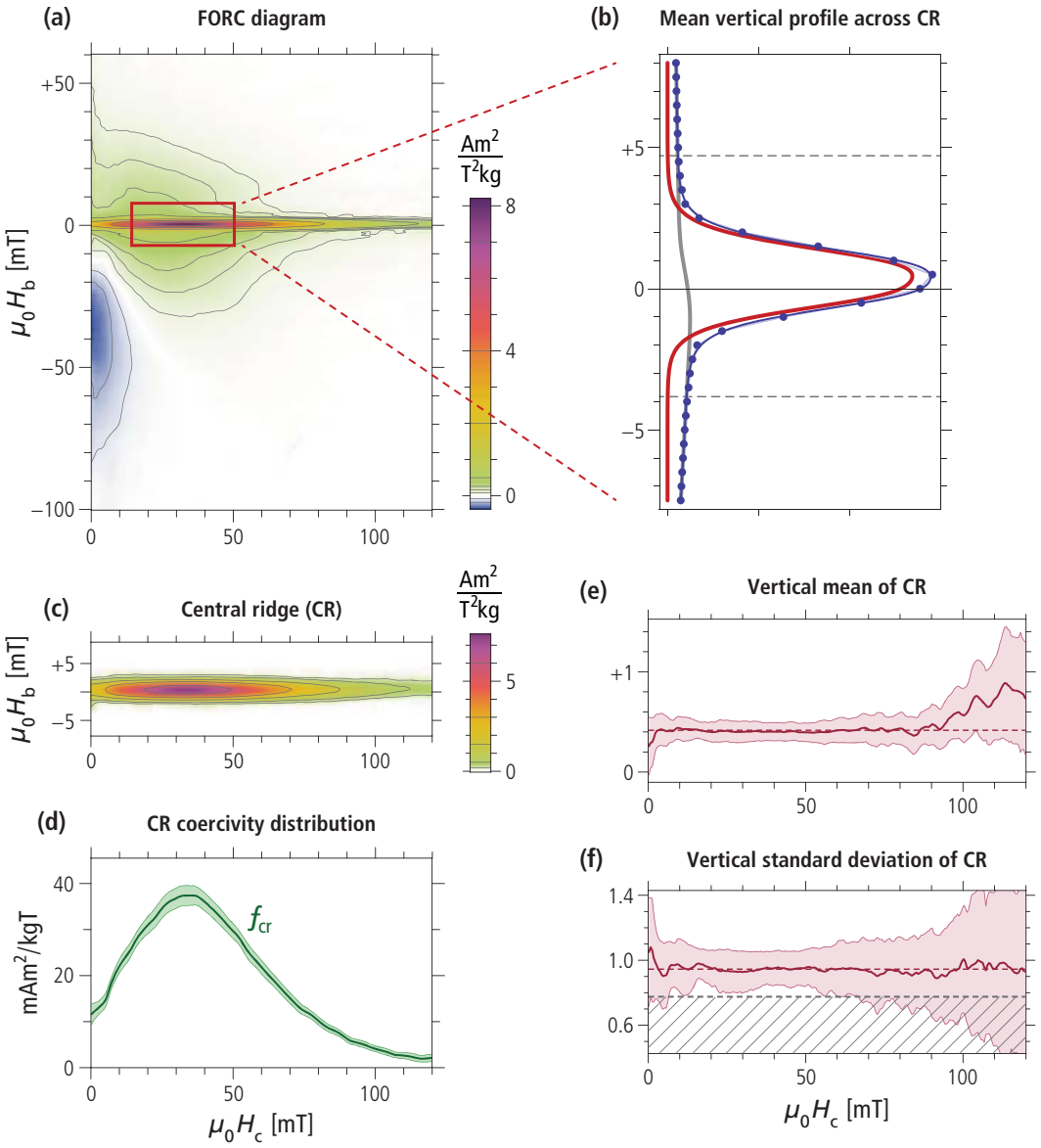

Plate 5. Central ridge analysis with `IsolateCR`. (a) FORC diagram obtained with **`CalculateFORC`** (contour lines have been added with **`PlotFORC`**). FORC data chosen by **`IsolateCR`** in order to calculate a mean vertical profile across the central ridge are outlined by the red rectangle. This selection corresponds to automatic options set with `INPUT 01` and `INPUT 02` in the parameter file `S0_VARIFORC_IsolateCR_parameters.txt`. **(b)** Mean vertical profile across the central ridge (dots), calculated from FORC data outlined in (a). The profile has been fitted with a model function for the central ridge (red) and for remaining FORC contributions (gray). Dashed lines delimit the H_b-range occupied by the central ridge. The fitted model provides the initial parameters used for analyzing all vertical profiles of the FORC diagram. **(c)** FORC diagram of the isolated central ridge, obtained from the analysis of vertical profiles as shown in (b). A 2× vertical exaggeration has been used, in order to highlight the ~0.4 mT vertical shift of the whole ridge above $\mu_0 H_b = 0$. **(d)** Central ridge coercivity distribution, f_{ir}, obtained by integrating the central ridge FORC diagram over H_b. The shaded band around f_{ir} is the estimated 2σ confidence level. **(e)** Vertical position of the central ridge as a function of H_c. Departure from the mean (dashed) at $\mu_0 H_c > 100$ mT is associated with a poor signal-to-noise ratio and is not significant. **(e)** Vertical standard deviation of the central ridge as a function of H_c. The hatched area marks standard deviations smaller than the minimum value σ_i associated with the vertical smoothing factor $s_b = 4$ used to process FORC measurements over the central ridge.

Complete VARIFORC analysis

FORC data processing with VARIFORC yields coercivity distributions and corresponding magnetizations derived from subsets of all FORC measurements. This additional information is important for establishing a link between FORC and conventional rock-magnetic parameters. As explained in the FORC tutorial provided with Chapter 8 of the VARIFORC user manual, three types of magnetization can be considered for this purpose: (1) the saturation remanence, M_{rs}, and the related coercivity distribution, f_{bk}, derived from backfield demagnetization data, (2) the irreversible component of the hysteresis loop, whose derivative with respect to the applied field defines a "coercivity distribution", f_{ir}, over positive and negative fields, with total magnetization M_{ir}, and (3) the coercivity distribution, f_{cr}, derived from the central ridge, with total magnetization M_{cr}.

In cases of FORC diagrams containing a central ridge, as in this example, quantitative analyses require proper ridge separation (Plate 6a-c). This operation is performed with **`IsolateCR`** exploitting the negligible intrinsic vertical extension of the central ridge, so that other FORC contributions can be linearly extrapolated under the range occupied by the ridge.

The FORC diagram remaining after subtraction of the central ridge (Plate 6b) features the typical signature of magnetic moment rotation in single-domain particles, which has been described by *Newell* [2005]. This signature consists of equal negative and positive amplitudes over the lower quadrant, which are symmetric about the $H_b = -H_c$ diagonal. On the other hand, positive contributions over the upper quadrant in Plate 6b, which represent ~45% of the total FORC magnetization, originate from a different source – possibly interacting single-domain or pseudo-single-domain particles [*Ludwig et al.*, 2013]. Interpretation ambiguities have been solved by comparing FORC measurements of the same material obtained before and after selective chemical dissolution of ultrafine magnetite particles of secondary origin, such as magnetofossils. Such comparison indicates that only 18% of the total FORC magnetization originates from primary minerals (see next sections).

Integrals of the coercivity distributions shown in Plate 6d yield the total magnetizations listed in Plate 6e. Corresponding magnetization ratios can be used for a quantitative description of the main FORC diagram characteristics: for example, $M_{ir}/M_{rs} \approx 1$ is expected for single-domain particles, and $M_{ir}/M_{rs} = \infty$ for ideal multidomain particles. Furthermore, M_{cr}/M_{rs} is a measure for the hysteresis loop squareness of particles associated with the central ridge, which depends on the magnetic switching mode (e.g., coherent rotation vs. fanning) and on the strength of thermal activations [*Ludwig et al.*, 2013]. All results shown in Plate 6 have been obtained with VARIFORC without additional processing.

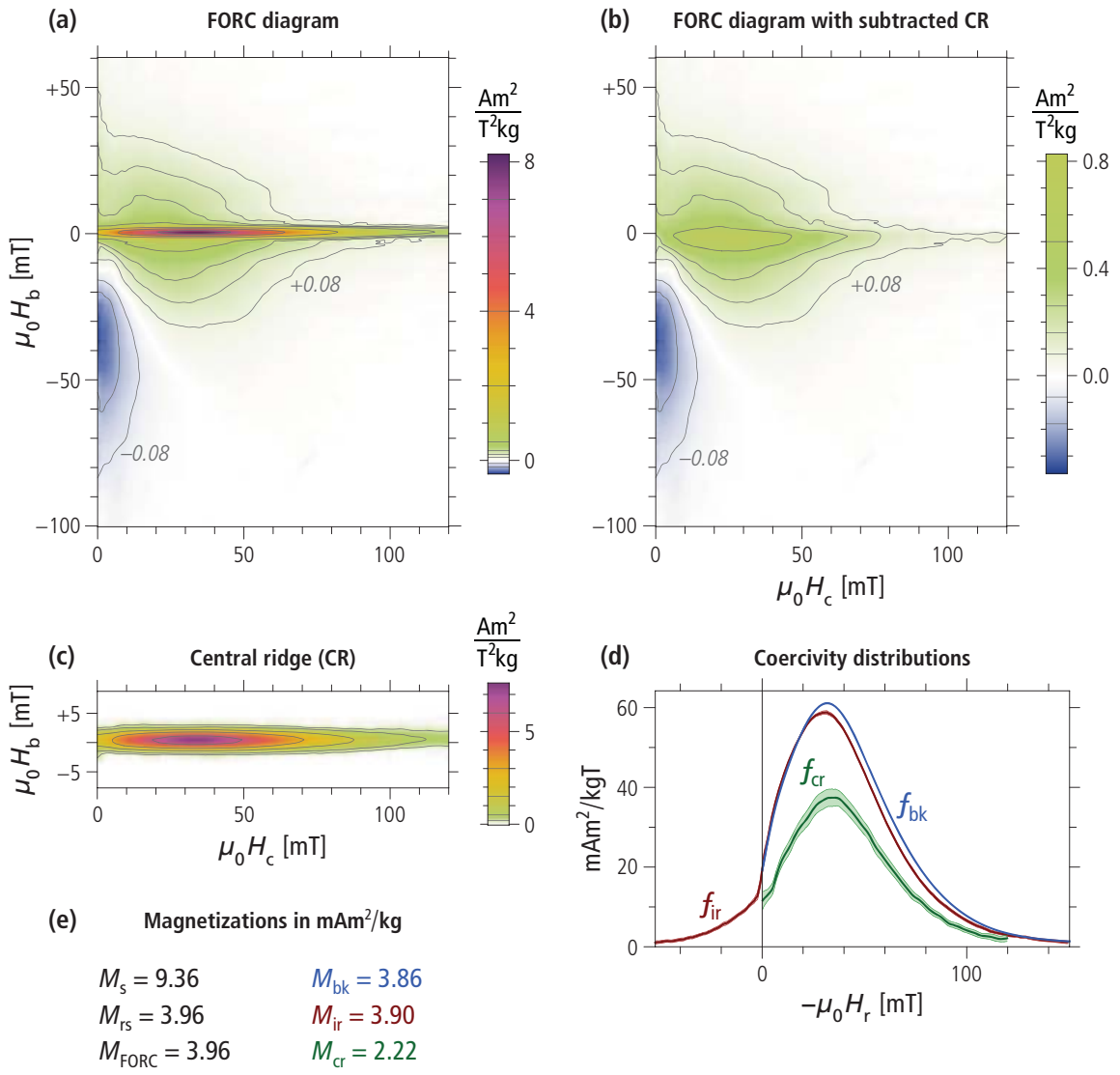

Plate 6. Complete VARIFORC analysis of a pelagic carbonate. (a) FORC diagram obtained with **CalculateFORC** (contour lines have been added with **PlotFORC**). Notice that the smallest contour level corresponds to 1% of the maximum FORC amplitude and is still fully significant. **(b)** FORC diagram remaining after subtraction of the central ridge with **IsolateCR**. The isolated central ridge is shown in **(c)** with a 2× vertical exaggeration, which highlights a small upward shift of the whole ridge. The shift is due to thermal activation effects and is a common feature for all sedimentary materials featuring a central ridge. All FORC diagrams share the same color scale. **(d)** Three types of coercivity distribution derived from FORC measurements with shaded bands around each curve representing 2σ confidence levels. The first two distributions, f_{bk} and f_{ir}, originate from FORC measurements in $H = 0$ and from the irreversible component of the lower branch of the hysteresis loop, respectively. They are generated by **CalculateFORC** as part of the standard output. The third distribution, f_{cr}, is associated with the central ridge and is generated by **IsolateCR**. All three distributions are plotted by **IsolateCR** as seen in this example. f_{ir} is the only distribution that exists for positive and negative fields, like the hysteresis loop from which it is derived. Negative arguments of f_{ir} originate from irreversible magnetization processes that occur without reversing the field direction. Only non-interacting, uniaxial single-domain particles produce a strictly positive f_{ir}. **(e)** Total magnetizations derived from FORC measurements (M_s and M_{rs}), integration of the FORC diagram (M_{FORC}), and integration of the coercivity distributions shown in (d) (M_{bk}, M_{ir}, and M_{cr}).

FORC analysis of selective chemical dissolution

As seen in the last section, the FORC signature of the magnetofossil-rich pelagic carbonates is compatible with non-interacting single-domain particles and another magnetic component whose origin is unclear. Although this signature is seen in all magnetofossil-bearing sediments, and the coercivity distributions of the central ridge appears to contain magnetofossil components [*Heslop et al.*, 2014], significant contributions from primary minerals, which might contain single-domain magnetic particles as well, cannot be excluded. A possible solution for untangling primary and secondary magnetic contributions consists in removing secondary magnetite particles by a citrate-bicarbonate-dithionite (CBD) treatment [*Ludwig et al.*, 2013], which is known to selectively dissolve magnetite particles smaller than a critical grain size comprised between 0.2 and 1 μm [*Hunt et al.*, 1995]. Because secondary magnetite particles are <1 μm in size, they will be completely removed by CBD. On the other hand, primary magnetites with much larger grain sizes, as well as primary single-domain particles embedded in a silicate matrix, will not be affected by CBD. Although ultra-fine primary (titano)magnetite from the low-end tail of a wide grain size distribution might be small enough to undergo chemical dissolution, experiments with different CBD treatment strengths yielded similar results. This result can be explained if dissolved and undissolved magnetic particles (1) originate from gran size distributions with little overlap, or (2) have different exposures to chemical dissolution, for instance by inclusion in other minerals [*Ludwig et al.*, 2013]. Therefore, differences between mass-normalized magnetic measurements of the same material before (bulk) and after (residue) CBD extraction can be identified with the original signature of secondary magnetite particles.

The calculation of FORC measurement differences is supported by the **`LinearCombineFORC`** module, which does not require any parameter input. Differences can be calculated in two ways: (1) by direct combination of corresponding pairs of measurements, if these were obtained from identical measurement protocols, or (2) by combination of FORC diagrams calculated over matching grids. In the first case, corrected measurement files created by **`ImportFORC`** are uploaded in **`LinearCombineFORC`** and combined with the coefficients +1 for the bulk, and −1 for the residue. In the second case, the same procedure is used with FORC matrix files created by **`CalculateFORC`** (see Chapter 7 of the VARIFORC user manual). In both cases, correct results are obtained only if measurements have been correctly normalized by specimen mass. Normalization by specimen mass, volume, or area, is supported by **`ImportFORC`** when uploading measurement files, whereby correct SI or cgs units are automatically generated.

The example shown in Plate 7 has been generated with **`LinearCombineFORC`** using averaged FORC measurements of bulk and residue calculated with **`ImportFORC`**. The CBD residue is ~5 times less magnetic than the bulk, and contains a significant fraction of high-coercivity minerals. Measurement differences resemble the bulk, however, closer inspection of Plate 6e-f shows that high-coercivity contributions are absent and the hysteresis loop becomes completely closed in field amplitudes >0.12 T. Further details can be seen on FORC diagrams, as discussed in the next section.

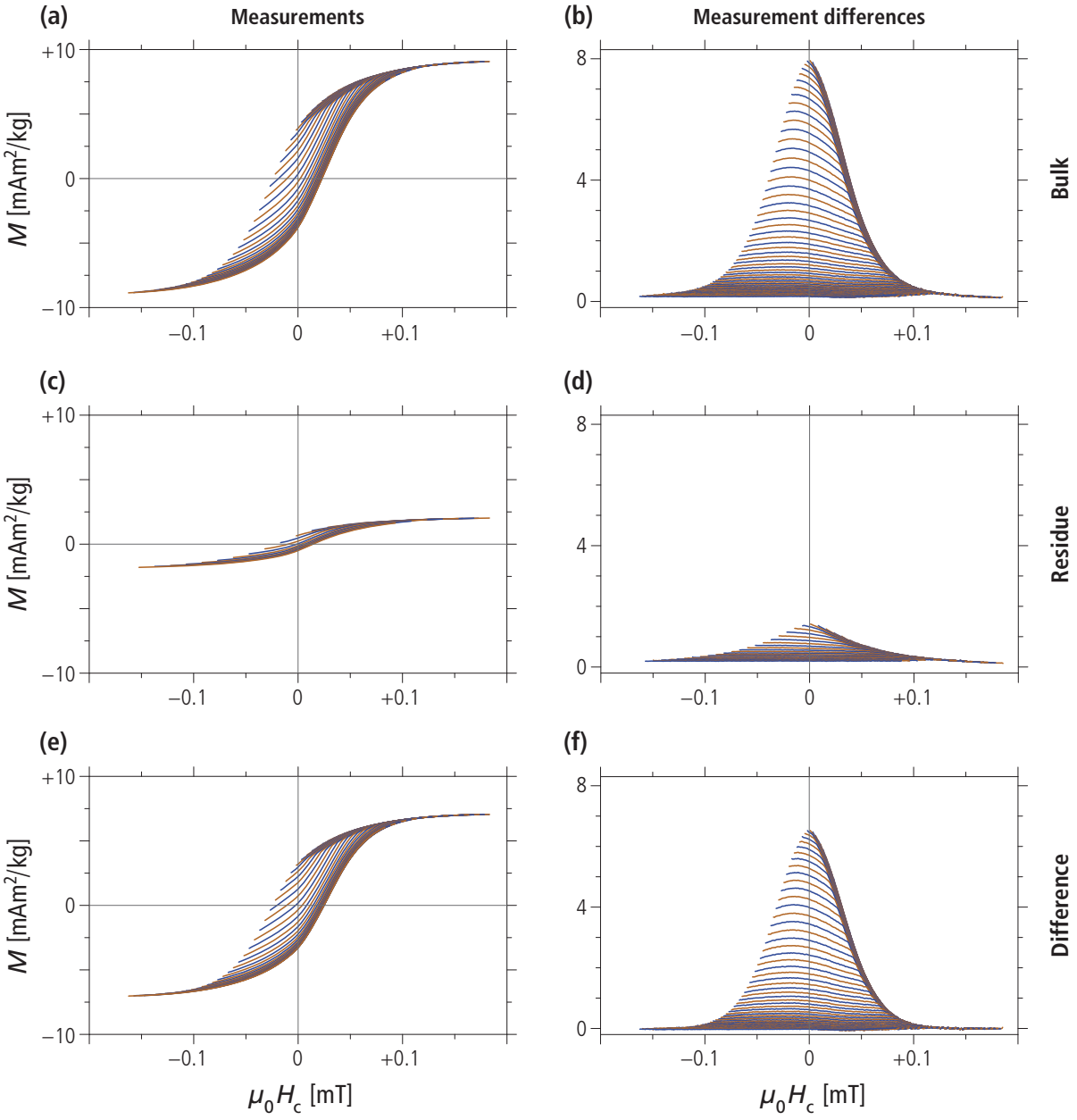

Plate 7. FORC measurements of untreated and CBD-treated material. (a-b) Corrected and averaged FORC measurements of the untreated material (bulk). **(c-d)** Corrected and averaged FORC measurements of the same material after selective CBD dissolution of ultrafine magnetite (residue). **(e-f)** Difference between bulk and residue, calculated with **`LinearCombineFORC`**. Plots on the left show as-measured FORC data. Plots on the right show the same data after subtraction of the lower branch of the hysteresis loop deduced from FORC measurements. Plot scales of bulk, residue, and difference are identical for better comparison.

FORC signature of primary minerals

As discussed in the previous section, the FORC signature of primary minerals can be identified with measurements of the CBD extraction residue. This signature is clearly distinct from the bulk (Plate 8). The FORC diagram contains a central ridge (Plate 8a), which has been analyzed with **`IsolateCR`**, obtaining the isolated ridge (Plate 8c), and the FORC diagram remaining after central ridge removal (Plate 8b). This analysis also yields the coercivity distributions shown in Plate 8d, and the corresponding magnetizations (Plate 8e).

Unlike the case of untreated sediment, the central ridge magnetization represents only 11% of the saturation remanence. The central ridge magnetization must originate from ferrimagnetic single-domain particles that have been protected from chemical dissolution, for example by embedment in a silicate matrix. The coercivity distribution f_{cr} of such particles (Plate 8d) is strongly affected by measurement noise; nevertheless, it appears to be significantly broader than the same distribution deduced from the bulk (Plate 6d), with coercivities extending well beyond 0.1 T. Pelagic carbonates from this region are known to contain volcanoclastic inputs from the Andes [*Straub and Schmincke*, 1998], and similar coercivity distributions are seen in volcanic material containing single-domain magnetite needles with low-Ti content [*Jackson et al.*, 2006].

The upper quadrant of the FORC diagram in Plate 8b does not contain contributions from single-domain particles related to the central ridge. This part of the diagram bears the typical FORC signature of ~2 μm pseudo-single-domain (titano)magnetite particles [*Muxworthy and Dunlop*, 2002].

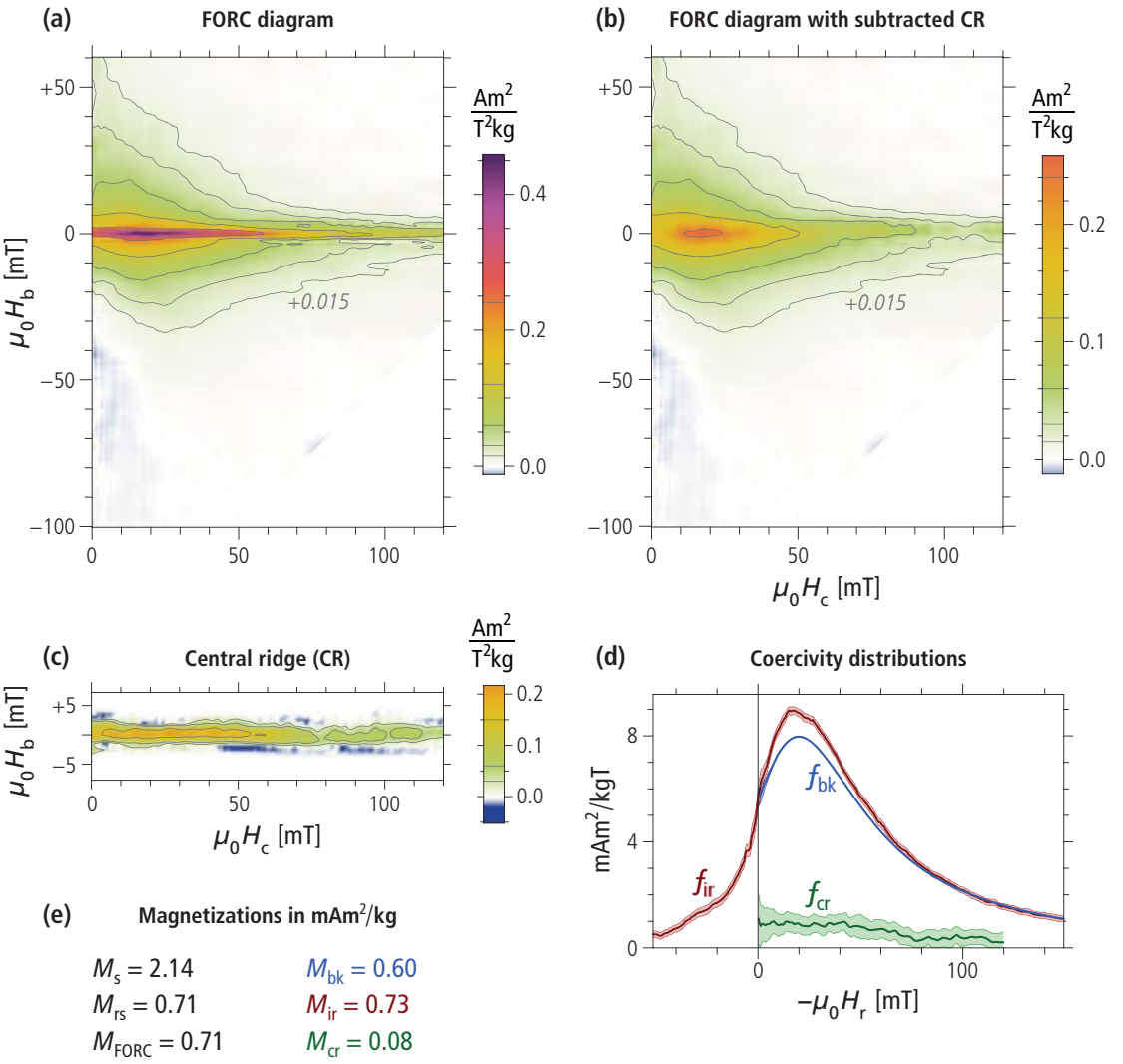

Plate 8. VARIFORC analysis of the pelagic carbonate's CBD-residue. (a) FORC diagram obtained with **`CalculateFORC`** (contour lines have been added with **`PlotFORC`**). Notice that the smallest contour level corresponds to 3% of the maximum FORC amplitude and is still fully significant. **(b)** FORC diagram remaining after subtraction of the central ridge with **`IsolateCR`**. The isolated central ridge is shown in **(c)** with a 2× vertical exaggeration, which highlights a small upward shift of the whole ridge. The shift is due to thermal activation effects and is a common feature for all sedimentary materials featuring a central ridge. All FORC diagrams share the same color scale. **(d)** Three types of coercivity distribution derived from FORC measurements, with shaded bands around each curve representing the 2σ confidence level. The first two distributions, f_{bk} and f_{ir}, originate from FORC measurements in $H = 0$ and from the irreversible component of the lower branch of the hysteresis loop, respectively. These coercivity distributions are generated by **`Calculate FORC`** as part of the standard output. The third distribution, f_{cr}, is associated with the central ridge and is generated by **`IsolateCR`**. All three distributions are plotted by **`IsolateCR`** as seen in this example. f_{ir} is the only distribution that exists for positive and negative fields, like the hysteresis loop from which it is derived. Negative arguments of f_{ir} originate from irreversible magnetization processes that occur without reversing the field direction. Only non-interacting, uniaxial single-domain particles produce a strictly positive f_{ir}. **(e)** Total magnetizations derived from FORC measurements (M_s and M_{rs}), integration of the FORC diagram (M_{FORC}), and integration of the coercivity distributions shown in (d) (M_{bk}, M_{ir}, and M_{cr}).

FORC signature of secondary minerals

As discussed in previous sections, the FORC signature of secondary minerals can be identified with the difference between mass-normalized measurements of the untreated material and the CBD extraction residue. This signature is similar to the bulk, given the small residue magnetization (Plate 9). As seen in plots of the FORC measurements (Plate 7, high-coercivity contributions are completely absent.

The central ridge is the dominant FORC diagram feature (Plate 9a,c), contributing to ~67% of the total FORC magnetization (Plate 9e). Negative amplitudes over the lower quadrant in Plate 9b match the typical signature of reversible magnetic moment rotation in single-domain particles [*Newell*, 2005], and are therefore associable with the central ridge. On the other hand, FORC contributions over the upper quadrant in Plate 9b must be attributed to interacting single-domain particles, in which case they might arise from collapsed magnetosome chains, or, alternatively, from small pseudo-single-domain particles. In the latter case, comparison with FORC measurements of synthetic samples suggests a particle size of ~0.3 μm [*Muxworthy and Dunlop*, 2002]. Magnetite particles of this size are dissolved by the CBD treatment and can therefore contribute to the FORC signature obtained from the difference between bulk and residue measurements. In this case, a secondary origin can be excluded, since magnetofossils [e.g. *Kopp and Kirschvink*, 2008], as well as authigenic magnetite precipitates [e.g. *Lovley et al.*, 1987; *Maher*, 1988; *Gibbs-Eggar et al.*, 1999], rarely exceed 0.1 μm in size. Primary particles of this size, on the other hand, would be part of a wide grain size distribution where the amount of extracted particles depend on the chemical extraction strength. Because the magnetization of extracted particle vary little over a range of extraction strengths [*Ludwig et al.*, 2013], a primary origin for the FORC signatures in Plate 9 can be excluded. Therefore, the most likely explanation for the upper quadrant of the FORC diagram in Plate 9b is given by magnetostatic interactions between single domain particles, possibly associated with collapsed magnetosome chains [*Li et al.*, 2012]. Very similar signatures are often seen in magnetofossil-rich sediments with small or completely absent detrital contributions [e.g., *Kind et al.*, 2011].

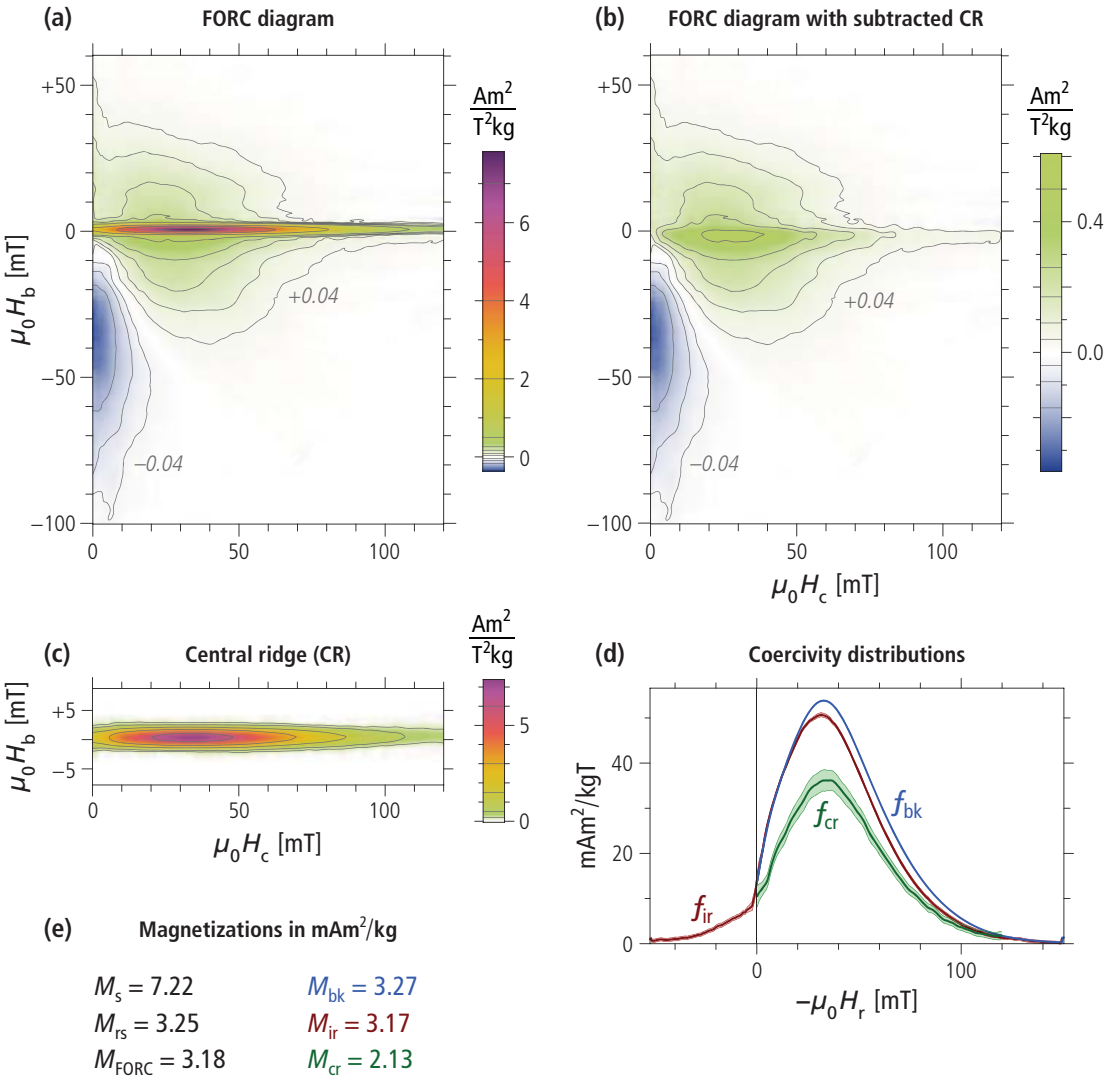

Plate 9. VARIFORC analysis of ultrafine magnetite extracted from the pelagic carbonate. (a) FORC diagram obtained with **`CalculateFORC`** (contour lines have been added with **`PlotFORC`**). Notice that the weakest contour level corresponds to 0.5% of the maximum FORC amplitude and is still fully significant. **(b)** FORC diagram remaining after subtraction of the central ridge with **`IsolateCR`**. The isolated central ridge is shown in **(c)** with a 2× vertical exaggeration, which highlights a small upward shift of the whole ridge. The shift is due to thermal activation effects and is a common feature for all sedimentary materials featuring a central ridge. All FORC diagrams share the same color scale. **(d)** Three types of coercivity distribution derived from FORC measurements, with shaded bands around each curve representing the 2σ confidence level. The first two distributions, f_{bk} and f_{ir}, originate from FORC measurements in $H = 0$ and from the irreversible component of the lower branch of the hysteresis loop, respectively. These coercivity distributions are generated by **`CalculateFORC`** as part of the standard output. The third distribution, f_{cr}, is associated with the central ridge and is generated by **`IsolateCR`**. All three distributions are plotted by **`IsolateCR`** as seen in this example. f_{ir} is the only distribution that exists for positive and negative fields, like the hysteresis loop from which it is derived. Negative arguments of f_{ir} originate from irreversible magnetization processes that occur without reversing the field direction. Only non-interacting, uniaxial single-domain particles produce a strictly positive f_{ir}. **(e)** Total magnetizations derived from FORC measurements (M_s and M_{rs}), integration of the FORC diagram (M_{FORC}), and integration of the coercivity distributions shown in (d) (M_{bk}, M_{ir}, and M_{cr}).

Literature

Abrajevitch, A., K. Kodama (2011). Diagenetic sensitivity of paleoenvironmental proxies: A rock magnetic study of Australian continental margin sediments, *Geochemistry, Geophysics, Geosystems 12*, Q05Z24, doi:101029/2010GC003481.

Abrajevitch, A., R.S. Hori, K. Kodama (2011). Magnetization carriers and remagnetization of bedded chert, *Earth and Planetary Science Letters 305*, 135-142, doi:10.1016/j.epsl.2011.02.047.

Chang, L., A.P. Roberts, M. Winklhofer, D. Heslop, M.J. Dekkers, W. Krijgsman, J.D. Fitz Gerald, P. Smith (2014). Magnetic detection and characterization of biogenic magnetic minerals: A comparison of ferromagnetic resonance and first-order reversal curve diagrams, *Journal of Geophysical Research: Solid Earth 119*, 6136-6158, doi:10.1002/2014JB011213.

Dunlop, D.J. (2002). Theory and application of the Day plot (M_{rs}/M_s versus H_{cr}/H_c) 2. Application to data for rocks, sediments, and soils, *Journal of Geophysical Research 107*, 2057, doi:10.1029/2001JB000487.

Egli, R. (2006). Theoretical aspects of dipolar interactions and their appearance in first-order reversal curves of thermally activated single-domain particles, *Journal of Geophysical Research 111*, B12S17, doi:10.1029/2006JB004567.

Egli, R., A.P. Chen, M. Winklhofer, K.P. Kodama, C.S. Horng (2010). Detection of noninteractinig single domain particles using first-order reversal curve diagrams, *Geochemistry, Geophysics, Geosystems 11*, Q01Z11, doi:101029/2009GC002916.

Egli, R. (2013). VARIFORC: An optimized protocol for calculating non-regular first-order reversal curve (FORC) diagrams, *Global and Planetary Change 110*, 302-320, doi:10.1016/j.gloplacha.2013.08.003.

Fabian, K., T. von Dobeneck (1997). Isothermal magnetization of samples with stable Preisach function: A survey of hysteresis, remanence, and rock magnetic parameters, *Journal of Geophysical Research 102*, 17659-17677.

Fabian, K. (2006). Approach to saturation analysis of hysteresis measurements in rock magnetism and evidence for stress-dominated magnetic anisotropy in young mid-ocean ridge basalt, Physics of the Earth and Planetary Interiors 154, 299-307.

Gehring, A.U., J. Kind, M. Charilaou, I. García-Rubio (2011). The detection of magnetotactic bacteria and magnetofossils by means of magnetic anisotropy, *Earth and Planetary Science Letters 309*, 113-117.

Geiss, C.E., R. Egli, and C.W. Zanner (2008). Direct estimates of pedogenic magnetite as a tool to reconstruct past climates from buried soils, *Journal of Geophysical Research 113*, B11102, doi:10.1029/2008JB005669.

Gibbs-Eggar, Z., B. Jude, J. Dominik, J.L. Loizeau, F. Oldfield (1999). Possible evidence for dissimilatory bacterial magnetite dominating the magnetic properties of recent lake sediments, *Earth and Planetary Science Letters 168*, 1-6.

Heslop, D., A.P. Roberts, L. Chang (2014). Characterizing magnetofossils from first-order reversal curve (FORC) central ridge signatures, *Geochemistry, Geophysics, Geosystems 15*, 2170-2179, doi:101002/2014GC005291.

Hunt, C.P., M.J. Singer, G. Kletetschka, J. TenPas, K.L. Verosub (1995). Effect of citrate-bicarbonate-dithionite treatment on fine-grained magnetite and maghemite, *Earth and Planetary Science Letters 130*, 87-94.

Jackson, M., B. Carter-Sitglitz, R. Egli, P. Solheid (2006). Characteriziing the superparamagnetic grain distribution $f(V,H_K)$ by thermal fluctuation tomography, *Journal of Geophysical Research 111*, B12S07, doi:10.1029/2006JB004514.

Kind, J., A.U. Gehring, M. Winklhofer, A.M. Hirt (2011). Combined use of magnetometry and spectroscopy for identifying magnetofossils in sediments, *Geochemistry, Geophysics, Geosystems 12*, Q08008, doi:101029/2011GC003633.

Kopp, R.E., and J.L. Kirschvink (2008). The identification and biogeochemical interpretation of fossil magnetotactic bacteria, *Earth-Science Reviews 86*, 42-61.

Li, J., W. Wu, Q. Liu, and Y. Pan (2012). Magnetic anisotropy, magnetostatic interactions, and identification of magnetofossils, *Geochemistry, Geophysics, Geosystems 13*, Q10Z51, doi:101029/2012GC004384.

Lin, W., Y. Pan (2009). Uncultivated magnetotactic cocci from Yuandadu Park in Beijing, China, *Applied and Environmental Microbiology 75*, 4046-4052.

Lovley, D.R., J.F. Stolz, G.L. Nord Jr., E.J.P. Phillips (1987). Anaerobic production of magnetite by a dissimilatory iron-reducing microorganism, *Nature 330*, 252-254.

Ludwig, P., R. Egli, S. Bishop, V. Chernenko, T. Frederichs, G. Rugel, S. Merchel, M.J. Orgeira (2013). Characterization of primary and secondary magnetite in marine sediment by combinding chemical and magnetic unmixing techniques, *Global and Planetary Change 110*, 321-339, doi:10.1016/j.gloplacha.2013.08.018.

Maher, B.A. (1988). Magnetic properties of some synthetic sub-micron magnetites, *Geophysical Journal 94*, 83-96.

Muxworthy, A.R., D.J. Dunlop (2002). First-order reversal curve (FORC) diagrams for pseudo-single-domain magnetites at high temperature, *Earth and Planetary Science Letters 203*, 369-382.

Muxworthy, A., W. Williams, D. Virdee (2003). Effect of magnetostatic interactions on the hysteresis parameters of single-domain and pseudo-single-domain grains, *Journal of Geophysical Research 108*, doi:10.1029/2003JB002588.

Newell, A.J. (2005). A high-precision model of first-order reversal curve (FORC) functions for single-domain ferromagnets with uniaxial anisotropy, *Geochemistry, Geophysics, Geosystems 6*, Q05010, doi:101029/2004GC000877.

Pan, Y., N. Petersen, M. Winklhofer, A.F. Davila, Q. Liu, T. Frederichs, M. Hanzlik, R. Zhu (2005). Rock magnetic properties of uncultured magnetotactic bacteria, *Earth and Planetary Sciences 237*, 311-325.

Pike, C.R., A.P. Roberts, M.J. Dekkers, K.L. Verosub (2001). An investigation of multi-domain hysteresis mechanisms using FORC diagrams, *Physics of the Earth and Planetary Interiors 126*, 11-25.

Roberts, A.P., L. Chang, D. Heslop, F. Florindo, J.C. Larrasoaña (2012). Searching for single domain magnetite in the "pseudo-single-domain" sedimentary haystack: Implications of biogenic magnetite preservation for sediment magnetism and relative paleointensity determination, *Journal of Geophysical Research 117*, B08104, doi:10.1029/2012JB009412.

Straub, S.M., H.U. Schmincke (1998). Evaluating the tephra input into Pacific Ocean sediments: distribution in space and time, *Geologische Rundschau 87*, 461-476.

Yamazaki, T., Y. Yamamoto, G. Acton, E.P. Guirdy, C. Richter (2013). Rock-magnetic artifacts on long-term relative paleointensity variations in sediments, *Geochemistry, Geophysics, Geosystems 14*, doi:101029/2012GC004546.